

High-Q TeO₂–Si Hybrid Microring Resonators

Khadijeh Mirabbas Kiani , Dawson B. Bonneville, Andrew P. Knights and Jonathan D. B. Bradley 

Department of Engineering Physics, McMaster University, 1280 Main Street West, Hamilton, ON L8S 4L7, Canada; bonnevdm@mcmaster.ca (D.B.B.); aknight@mcmaster.ca (A.P.K.); jbradley@mcmaster.ca (J.D.B.B.)

* Correspondence: miarabbk@mcmaster.ca

Abstract: We present the design and experimental measurement of tellurium oxide-clad silicon microring resonators with internal Q factors of up to 1.5×10^6 , corresponding to a propagation loss of 0.42 dB/cm at wavelengths around 1550 nm. This compares to a propagation loss of 3.4 dB/cm for unclad waveguides and 0.97 dB/cm for waveguides clad with SiO₂. We compared our experimental results with the Payne–Lacey model describing propagation dominated by sidewall scattering. We conclude that the relative increase in the refractive index of TeO₂ reduces scattering sufficiently to account for the low propagation loss. These results, in combination with the promising optical properties of TeO₂, provide a further step towards realizing compact, monolithic, and low-loss passive, nonlinear, and rare-earth-doped active integrated photonic devices on a silicon photonic platform.

Keywords: silicon-on-insulator (SOI); silicon photonics; optical microrings; tellurium oxide



Citation: Mirabbas Kiani, K.; Bonneville, D.B.; Knights, A.P.; Bradley, J.D.B. High-Q TeO₂–Si Hybrid Microring Resonators. *Appl. Sci.* **2022**, *12*, 1363. <https://doi.org/10.3390/app12031363>

Academic Editor: Joan Manel Ramírez

Received: 12 January 2022

Accepted: 25 January 2022

Published: 27 January 2022

Publisher's Note: MDPI stays neutral with regard to jurisdictional claims in published maps and institutional affiliations.



Copyright: © 2022 by the authors. Licensee MDPI, Basel, Switzerland. This article is an open access article distributed under the terms and conditions of the Creative Commons Attribution (CC BY) license (<https://creativecommons.org/licenses/by/4.0/>).

1. Introduction

The impact of silicon photonics on the development of photonic integrated circuits (PICs) is considerable, because of device compatibility with complementary metal–oxide–semiconductor (CMOS) technology and the leveraging of decades of research stimulated by the microelectronics industry [1]. The miniaturization of photonic waveguides has emerged as one of the most prominent technology platforms for PICs in recent decades [2].

The reduction in propagation loss associated with silicon waveguides is an ongoing research area because loss is a key parameter for link budget management in on-chip optical networks and many important micro-photonic devices, as well as passive and active systems including sensors, filters, delay lines, and light sources [3–6]. One device structure for which propagation loss is particularly critical is the microring resonator (MRR). MRRs provide an efficient cavity which has a compact size, wavelength selectivity, tunability, scalability, and functional versatility [7], making them a prominent candidate for a variety of applications including lasers [8,9], optical sensors [10], nonlinear optics [11,12], quantum optics [13], (de-)multiplexing systems [14], optical filters [15], and optical modulators [16]. The loss in MRRs can be quantified by the cavity Q factor, which is typically limited to values on the order of 10^5 in standard 220 nm-high single-mode silicon MRRs around 1550 nm.

Several approaches have been explored for enhancing the Q factor in silicon MRRs, including minimizing light scattering at roughened sidewalls via shallow-etched or multi-mode waveguide designs and alternative fabrication methods based on selective oxidation, e-beam lithography, reactive ion plasma etching, inductively coupled plasma (ICP) etching, or low-pressure chemical vapor deposition (LPCVD). High- Q factor silicon MRRs fabricated using a selective oxidation process have been shown with intrinsic Q factors of 5.1×10^5 [17] and 7.6×10^5 [18], although challenges remain in the control of the fabrication process [19]. A silicon microring resonator with a Q factor of 1.7×10^6 was demonstrated using a large cross-section multi-mode waveguide with a severely limited free spectral range (FSR) of 17.1 pm [20]. With a similar approach, a silicon microring resonator with a high Q of 1.3×10^6 and larger FSR was proposed in [21], with a bend radius of 450 μ m. A silicon MRR

with an internal Q factor of 1.1×10^6 and FSR of 0.208 nm and utilizing a multi-mode ridge waveguide was fabricated using a standard CMOS-compatible silicon-on-insulator (SOI) process [22]. A multi-mode ultrahigh quality factor racetrack resonator with a 1.6 μm width was proposed using a standard single-etching process with a quality factor of 2.3×10^6 provided by a multi-project wafer foundry [23]. An internal quality factor of 2.2×10^7 , corresponding to a 2.7 dB/m propagation loss, was achieved in a silicon microring resonator with a radius of 2.45 mm cladded with silicon oxide [24] by oxidizing the wafer surface in a steam oxidation process and using a reflowing photoresist strategy. An intrinsic Q factor of 1.57×10^6 , corresponding to a waveguide loss of 0.35 dB/cm, was realized in a silicon MRR with a radius of 150 μm and an FSR of 0.845 nm using e-beam lithography with a top cladding of a glass-like compound from hydrogen silsequioxane (HSQ) covered with a silicon oxide layer [25]. Low-loss submicron silicon-on-insulator strip waveguides were reported with a 0.5 dB/cm loss at 1310 nm and a 30 μm bend radius, cladded with silicon oxide [26] using H_2 plasma post-lithography treatment and H_2 thermal annealing after silicon etching. More generally, propagation losses lower than 0.4 dB/cm for the C-band and 0.8 dB/cm for the O-band of silicon wire waveguides have been reported for waveguides with a 440 nm core width, 220 nm core height, and 2 μm -thick SiO_2 cladding layer defined by a high-resolution immersion lithography process [27]. While all of these approaches to improving Q factors in silicon MRRs are promising for different applications, they either suffer from performance trade-offs (e.g., multi-mode operation, larger footprint, and/or significantly reduced FSR) or add fabrication cost and complexity.

In this paper, we demonstrate a silicon MRR with a Q factor of 1.5×10^6 at 1550 nm, corresponding to a propagation loss of 0.42 dB/cm, fabricated with a standard foundry process, plus a low-temperature post-process deposition of a TeO_2 cladding layer. In addition to enabling a straightforward and monolithic low-loss hybrid waveguide structure, TeO_2 has promising optical properties for new functionalities in silicon photonic microsystems. TeO_2 has been shown to be thermally and chemically stable, possess high nonlinearity, and low optical attenuation from visible to mid-infrared wavelengths (0.4–5 μm), and have a high refractive index (2.1 at 1550 nm) and low dispersion [28]. Furthermore, the unique site variability in the TeO_2 glass matrix enables high rare-earth dopant solubility and leads to large emission bandwidths, motivating its application in integrated optical amplifiers and lasers [29–31], including the recent demonstration of a hybrid rare-earth laser directly on silicon with an internal quality factor of 5.6×10^5 [32]. This low-loss platform has significant potential for linear, nonlinear, and active optical applications in silicon photonics.

2. Microring Resonator Fabrication and Design

The microring resonator structure used in this work is displayed in Figure 1. It consists of an integrated silicon microring and bus waveguide coated with a thin film of tellurium oxide (TeO_2). The silicon structure was fabricated in a silicon photonics foundry on a wafer-scale SOI platform with a 220 nm silicon layer thickness and consists of a 30 μm -radius silicon microring constructed using a 0.5 μm -wide waveguide. The bus waveguide is 0.4 μm wide, and the point coupling gap is 1.0 μm . The structure was cladded with SiO_2 , and subsequently, a window on top of the microring resonator was etched to the silicon layer for use in the post-processing TeO_2 deposition or unclad device experiments. A set of devices with identical dimensions but without the SiO_2 cladding etched was also fabricated for comparison. Deep etching was used for end-facet preparation and wafer dicing. For the TeO_2 -clad devices, the structure was coated with a 270 nm-thick TeO_2 film deposited using a room-temperature reactive RF co-sputtering post-processing step with 145 W of tellurium target sputtering power, 2.8 mTorr chamber pressure, and 12 and 7.6 sccm of argon and oxygen flow, respectively. The substrate temperature was set at 20 °C. A top-view scanning electron microscope (SEM) image and the cross-section diagram of the TeO_2 -coated Si microring resonator are displayed in Figure 1a,b, respectively. Figure 1c,d show the image

of the experimental setup and a microscopic image of the microring resonator with an open window structure.

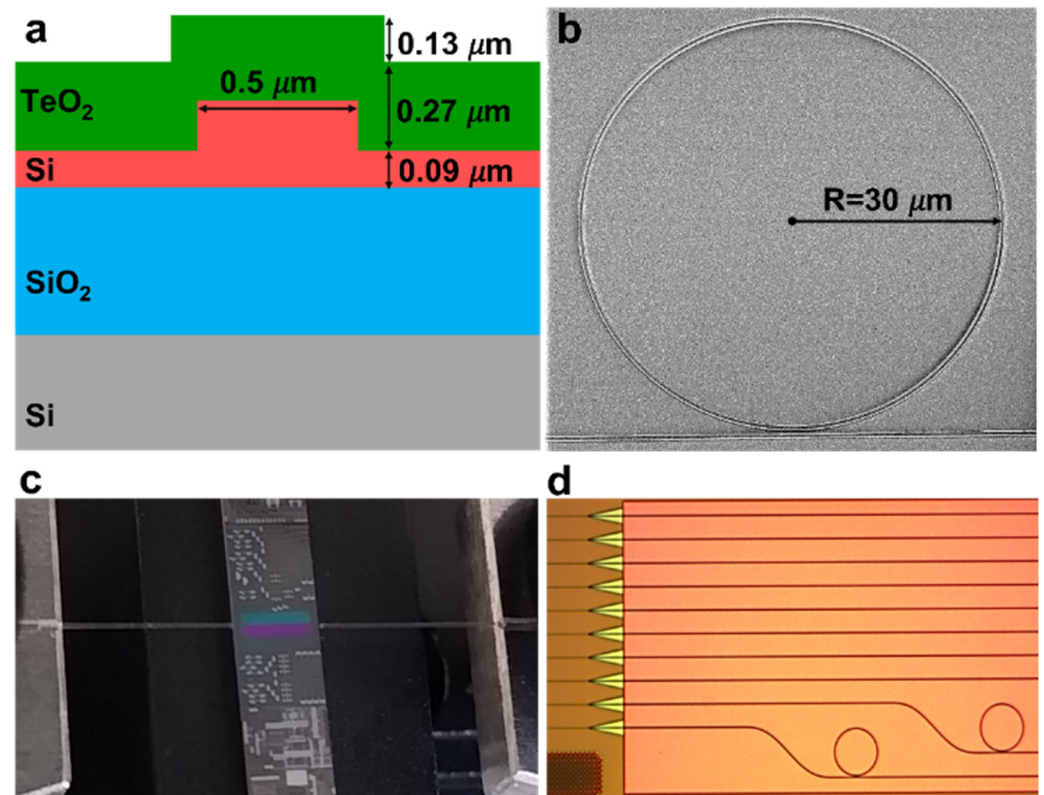


Figure 1. (a) Cross-section profile of the TeO₂-coated Si microring showing the microring structure. (b) Top-view SEM image of a TeO₂-coated Si microring resonator. (c) Photograph of the coupling setup during measurement showing the SOI chip with window opening for TeO₂ post-processing deposition. (d) Microscopic image of the open window microring resonator structure.

The electric field profiles of the transverse-electric (TE)-polarized fundamental modes calculated using a finite element method (FEM) modesolver for the (cladding–core) TeO₂–Si, SiO₂–Si, and air–Si waveguides at a 1550 nm wavelength are displayed in Figure 2a–c, respectively. We also summarize the calculated optical properties of the TeO₂–Si, SiO₂–Si, and air–Si microring resonator structures in Figure 2d. The microring resonators and the bus waveguides were designed to achieve single-mode waveguide conditions at 1.55 to 2 μm wavelengths. The ring waveguide structure supports the TE-polarized and TM-polarized modes, and it has a low bending radiation loss at 1550 nm for TE only. The effective index of the TeO₂-coated resonator is 2.8, which is almost 7.7 and 12% higher than that of the air- and SiO₂-clad devices. For the TeO₂-coated Si microring resonator, 21.7% of the optical power is confined in the TeO₂ coating layer, while 65.0% is confined in the silicon layer. The rest of the optical power is confined in the lower SiO₂ cladding. Slightly lower cladding confinement of 15.8 and 17.2%, respectively, is observed in the air- and SiO₂-clad cases. The effective area is slightly larger in the TeO₂-coated Si microring resonator than SiO₂-coated and uncoated silicon microring resonators, although the mode is pulled upward more into the cladding, both of which can influence the ring–bus waveguide coupling.

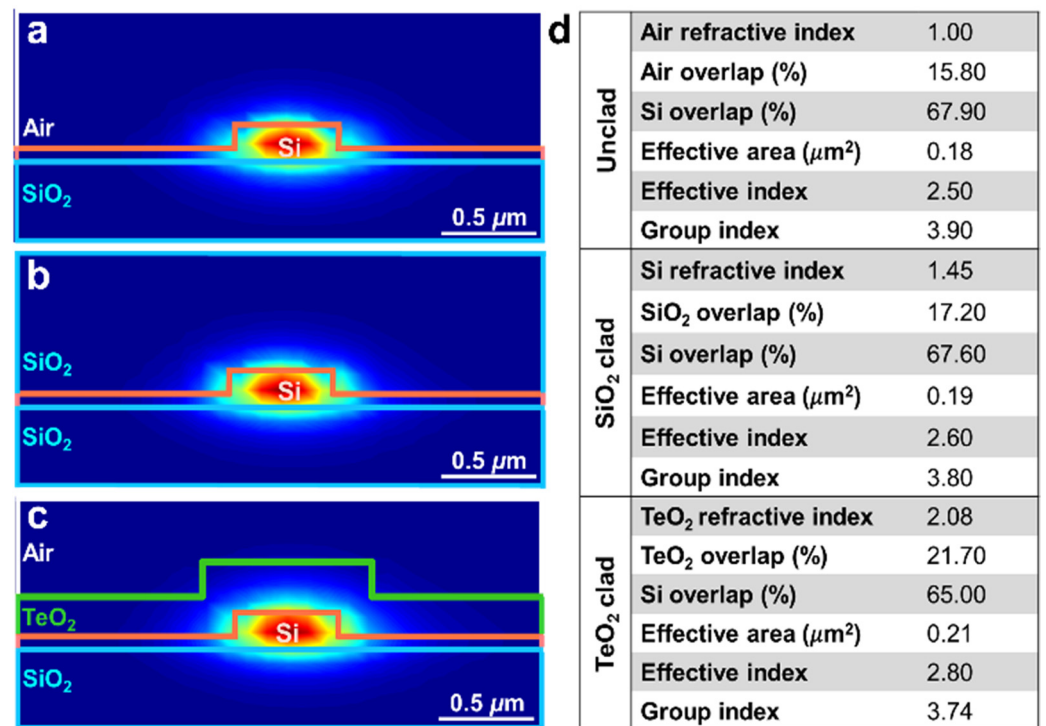


Figure 2. Calculated electric field profile of the fundamental transverse-electric (TE)-polarized mode for (a) unclad, (b) SiO₂-clad, and (c) TeO₂-clad silicon microring resonators. (d) Calculated fractional optical intensity overlap factors and effective mode areas for the fundamental TE microring mode at 1550 nm wavelength.

The TeO₂-coated resonator has a higher mode area of approximately $0.20 \mu\text{m}^2$ at $1.55 \mu\text{m}$. The effective index increases for the TeO₂ film cladding as the resonant mode becomes more confined in the TeO₂ layer. The expansion of the optical mode at longer wavelengths decreases the effective index. The results show that approximately 60% of the mode power is confined in the Si region and 26% in the TeO₂-cladded layer for the TeO₂ cladding at a wavelength of $1.55 \mu\text{m}$.

3. Microring Resonator Characterization

We used a fiber-chip edge coupling setup, a tunable Agilent 81640A 1510–1640 nm laser, and a fiber probe station to characterize the passive transmission properties of the silicon microring resonators. TE-polarized light from a 1550 nm tunable laser was launched into the chip through the polarization controller and lensed fiber, and the transmitted light across the chip was launched to the output lensed fiber connected to the Agilent power sensor. We observed TE single-mode resonances supported by the microring resonator, as shown in Figure 3a–c. For the TeO₂-coated silicon microring resonator, we measured a free spectral range (FSR) of 3.7 nm at a wavelength of 1573 nm. The air- and SiO₂-clad devices were under-coupled over the measured transmission range, while the TeO₂-clad MRR was under-coupled at shorter wavelengths and became critically coupled above $\sim 1600 \text{ nm}$. By fitting the transmission responses of the under-coupled resonator using a Lorentzian function (as indicated in Figure 3d–f), we obtained internal quality factors, Q_i , of 2.0×10^5 at 1542.43 nm, 6.7×10^5 at 1587.28 nm, and 1.5×10^6 at 1579.94 nm for the uncoated, SiO₂-coated, and TeO₂-coated silicon MRRs, respectively, corresponding to 3.4 dB/cm, 0.97 dB/cm, and 0.42 dB/cm propagation losses in the microring [33]. The results are summarized in Table 1, including the TeO₂ film loss measured by prism coupling on a witness sample, showing low material loss, and fitted external and internal Q factors for the MRRs with different top claddings.

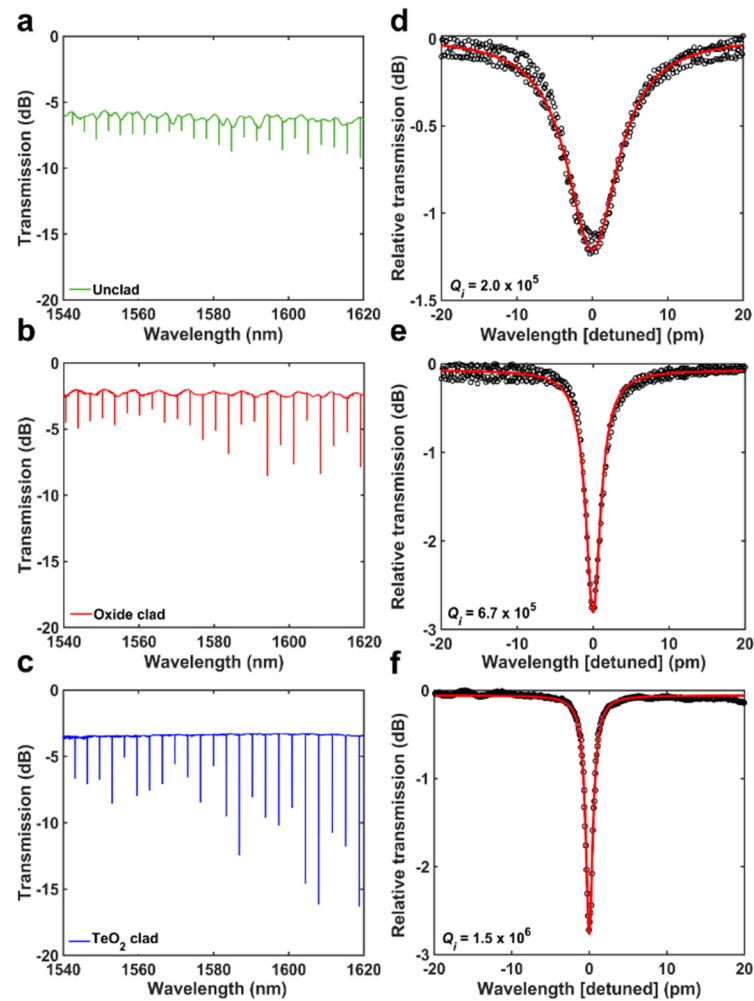


Figure 3. Measured TE transmission spectra for (a) uncoated, (b) SiO₂-coated, and (c) TeO₂-coated silicon microring resonators with a microring–waveguide gap of 1.0 μm. Close-up views of the under-coupled resonances for the (d) uncoated, (e) SiO₂-coated, and (f) TeO₂-coated silicon microring resonators showing an intrinsic quality factor, Q_i , of 1.5×10^6 , corresponding to 0.42 dB/cm optical propagation loss for the TeO₂-coated silicon microring resonator.

Table 1. Measured properties of silicon microring resonators with different cladding materials.

Cladding Material	Cladding Thickness (nm)	Film Loss @ 638 nm (dB/cm)	Film Loss @ 1550 nm (dB/cm)	Extinction Ratio (dB)	External Q Factor	Internal Q Factor	Propagation Loss (dB/cm)
Uncladded	—	—	—	1.2	2.8×10^6	2.0×10^5	3.4
SiO ₂	2000	—	—	2.8	4.2×10^6	6.7×10^5	0.97
TeO ₂	270	0.5 ± 0.2	0.1 ± 0.1	2.8	9.0×10^6	1.5×10^6	0.42

The total loss in the MRR can be expressed as the losses from the bulk materials, including contributions from the Si, SiO₂, and TeO₂ linear absorption and Si nonlinear (two-photon) absorption, radiation loss due to waveguide bends, and surface scattering losses related to the waveguide surface roughness and geometry. The bulk loss includes losses from impurities, internal defects, absorption loss due to chemical bonds, and nano- and micro-voids. Because of the high-quality silicon-on-insulator and SiO₂ foundry materials, and low TeO₂ film loss, we expected the bulk material loss contribution to be negligible. Furthermore, nonlinear optical loss was anticipated to be low due to the low power used in the transmission experiments.

We calculated the theoretical radiation loss and equivalent Q factor for the TeO_2 -coated silicon microring resonator structure using an FEM bent eigenmode solver, for varying bend radii, as shown in Figure 4a. The dashed lines in Figure 4a indicate the experimentally determined internal Q factors for the MRRs with different claddings. The calculated radiation-limited Q factors were measured to be 3×10^8 , 1×10^8 , and 1.7×10^7 for the TeO_2 -clad, SiO_2 -clad, and unclad microring resonators, respectively, at a radius of $30 \mu\text{m}$, corresponding to 0.002 dB/cm , 0.007 dB/cm , and 0.04 dB/cm propagation losses. The results show that the radiation loss was low ($Q > 10^7$) at the selected bend radius of $30 \mu\text{m}$.

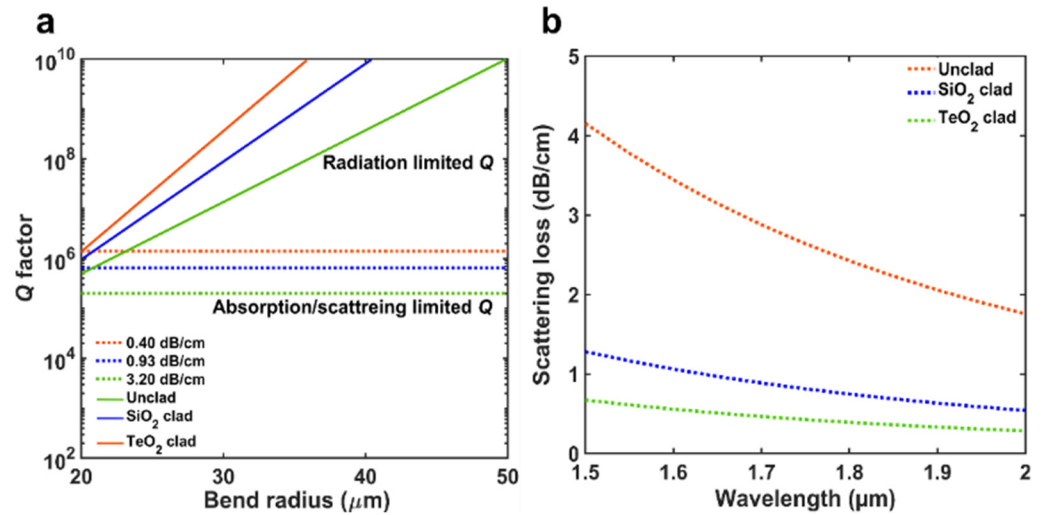


Figure 4. (a) Calculated internal Q factor of uncoated-, SiO_2 -coated, and TeO_2 -coated silicon resonator waveguides versus bend radius. (b) Calculated scattering loss as a function of wavelength for microring resonators with air, SiO_2 , and TeO_2 claddings based on the 3D Payne–Lacey model.

The surface scattering loss is the waveguide scattering loss per unit length and was calculated using the widely used Payne–Lacey model [34]. This model has been applied previously to 3D-SOI bent waveguides [35–37] such that

$$\alpha_{Surface\ Scattering} = 4.34 \frac{\sigma^2}{\sqrt{2}k_0 \left(\frac{W}{2}\right)^4 n_1} f \cdot g \cdot \eta \tag{1}$$

where σ , k_0 , W , and n_1 are the roughness, free-space wave vector, waveguide width, and core index, respectively. The function f is determined by the correlation length (L_c), while g is determined by the geometry of the waveguide and accounts for ridge-type waveguide structures such as the SOI ridge rings investigated here. Both σ and L_c are typically measured via atomic force microscopy or scanning electron microscopy of a waveguide. We assumed values of 1.0 nm and 50 nm for σ and L_c , respectively, based on previous measurements on SOI waveguides [35–38]. We also assumed the roughness of the TeO_2 coating can be neglected based on previous AFM roughness measurements showing $<1 \text{ nm}$ root mean square (RMS) surface roughness on low-loss sputtered thin films [38]. Details of the expressions g and f can be found in the Payne–Lacey model [34]. The Payne–Lacey model was modified for bent waveguides and rings by adding a correction factor η [35] which allows us to accurately predict the loss of bent waveguides or resonators given the value of the sidewall roughness. The correction factor η is defined as the ratio of the mode overlap between bent and straight waveguides using an FEM simulation. In the Payne–Lacey bending model, η is considered 1 in the straight waveguide. We plot the sidewall scattering loss as a function of the wavelength in Figure 4b. The experimental loss obtained from the quality factor measurements of the MRRs follows the same trend as the Payne–Lacey model, which indicates that the losses in the different MRRs are largely

influenced by the core cladding refractive index contrast and sidewall roughness [23]. These results show that the application of a high-refractive-index TeO₂ top cladding can be considered promising for low-loss passive components as well as active devices such as monolithic amplifiers and lasers with improved performance on the SOI platform [32].

4. Conclusions

In summary, we have demonstrated a compact, single-mode TeO₂-Si hybrid microring resonator with a 1.5×10^6 internal Q factor corresponding to a 0.42 dB/cm propagation loss. The resonator was fabricated using a standard wafer-scale foundry process and a simple post-processing TeO₂ deposition step at room temperature. We propose that these results on tellurium oxide-coated silicon microring resonators are promising for the fabrication of integrated on-chip low-cost and high-performance rare-earth-doped active devices such as amplifiers and lasers, as well as low-loss passive and nonlinear devices in silicon photonic platforms, with signal processing, light generation, microwave photonics, environmental and biological sensing, and communications applications.

Author Contributions: K.M.K. designed the device; K.M.K. and D.B.B. laid out the silicon chips. K.M.K. developed the low-loss tellurium oxide films on the silicon chips. K.M.K. performed the experimental characterization and analysis. K.M.K. wrote the original manuscript. A.P.K. and J.D.B.B. reviewed and edited the text. A.P.K. and J.D.B.B. supervised the project. All authors have read and agreed to the published version of the manuscript.

Funding: This research was funded by the Natural Sciences and Engineering Research Council of Canada (grant numbers RGPIN-2017-06423, STPGP 494306, and RTI-2017-00474), the Canadian Foundation for Innovation (CFI project number 35548), and the Ontario Research Fund (ORF project numbers 35548 and RE-09-051).

Institutional Review Board Statement: Not applicable.

Informed Consent Statement: Not applicable.

Data Availability Statement: The data presented in this study are available on request from the corresponding author.

Acknowledgments: We thank CMC Microsystems and the SiEPIC Program for facilitating the silicon photonics fabrication, and the Centre for Emerging Device Technologies (CEDT) at McMaster University for support with the reactive sputtering system.

Conflicts of Interest: The authors declare no conflict of interest.

References

1. Thomson, D.; Zilkie, A.; Bowers, J.E.; Komljenovic, T.; Reed, G.T.; Vivien, L.; Marris-Morini, D.; Cassan, E.; Viot, L.; Fédéli, J.-M.; et al. Roadmap on silicon photonics. *J. Opt.* **2016**, *18*, 073003. [[CrossRef](#)]
2. Baets, R.; Subramanian, A.Z.; Clemmen, S.; Kuyken, B.; Bienstman, P.; Le Thomas, N.; Roelkens, G.N.; Van Thourhout, D.; Helin, P.; Severi, S. Silicon Photonics: Silicon nitride versus silicon-on-insulator. In Proceedings of the Optical Fiber Communications Conference and Exhibition, Anaheim, CA, USA, 20–22 March 2016.
3. Watts, M.R.; Shaw, M.J.; Nielson, G.N. Optical Resonators: Microphotonic Thermal Imaging. *Nat. Photonics* **2007**, *1*, 632. [[CrossRef](#)]
4. Tran, M.A.; Huang, D.; Komljenovic, T.; Peters, J.; Malik, A.; Bowers, J.E. Ultra-Low-Loss Silicon Waveguides for Heterogeneously Integrated Silicon/III-V Photonics. *Appl. Sci.* **2018**, *8*, 1139. [[CrossRef](#)]
5. Xiang, C.; Jin, W.; Guo, J.; Williams, C.; Netherton, A.M.; Chang, L.; Morton, P.A.; Bowers, J.E. Effects of nonlinear loss in high-Q Si ring resonators for narrow-linewidth III-V/Si heterogeneously integrated tunable lasers. *Opt. Express* **2020**, *28*, 19926–19936. [[CrossRef](#)] [[PubMed](#)]
6. Biberman, A.; Bergman, K. Optical interconnection networks for high performance computing system. *Rep. Prog. Phys.* **2012**, *75*, 046402. [[CrossRef](#)]
7. Xiao, S.; Khan, M.H.; Shen, H.; Qi, M. Multiple-channel silicon micro-resonator-based filters for WDM applications. *Opt. Express* **2007**, *15*, 7489–7498. [[CrossRef](#)] [[PubMed](#)]
8. Salih Magden, E.; Li, N.; Purnawirman; Bradley, J.D.B.; Singh, N.; Ruocco, A.; Petrich, G.S.; Leake, G.; Coolbaugh, D.D.; Ippen, E.P.; et al. Monolithically-integrated distributed feedback laser compatible with CMOS processing. *Opt. Express* **2017**, *25*, 18058–18065. [[CrossRef](#)] [[PubMed](#)]

9. Stern, B.; Ji, X.; Dutt, A.; Lipson, M. Compact narrow-linewidth integrated laser based on a low-loss silicon nitride ring resonator. *Opt. Lett.* **2017**, *42*, 4541–4544. [[CrossRef](#)] [[PubMed](#)]
10. Sun, Y.; Fan, X. Optical ring resonators for biochemical and chemical sensing. *Analytical and Bioanalytical Chemistry. Anal. Bioanal. Chem.* **2011**, *399*, 205–211. [[CrossRef](#)] [[PubMed](#)]
11. Ji, M.; Cai, H.; Deng, L.; Huang, Y.; Huang, Q.; Xia, J.; Li, Z.; Yu, J.; Wang, Y. Enhanced parametric frequency conversion in a compact silicon-graphene microring resonator. *Opt. Express* **2015**, *23*, 18679–18685. [[CrossRef](#)] [[PubMed](#)]
12. Mirabbas Kiani, K.; Mbonde, H.M.; Frankis, H.C.; Mateman, R.; Leinse, A.; Knights, A.P.; Bradley, J.D.B. Four-wave mixing in high-Q tellurium-oxide-coated silicon nitride microring resonators. *OSA Contin.* **2020**, *3*, 3497–3507. [[CrossRef](#)]
13. Grassani, D.; Azzini, S.; Liscidini, M.; Galli, M.; Strain, M.J.; Sorel, M.; Sipe, J.E.; Bajoni, D. Micrometer-scale integrated silicon source of time-energy entangled photons. *Optica* **2015**, *2*, 88–94. [[CrossRef](#)]
14. La Notte, M.; Troia, B.; Muciaccia, T.; Campanella, C.E.; De Leonardi, F.; Passaro, V.M. Recent advances in gas and chemical detection by Vernier effect-based photonic sensors. *Sensors* **2014**, *14*, 4831–4855. [[CrossRef](#)] [[PubMed](#)]
15. Rabus, D.G.; Hamacher, M.; Troppenz, U.; Heidrich, H. Optical filters based on ring resonators with integrated semiconductor optical amplifiers in GaInAsP-InP. *IEEE. J. Sel. Top. Quant.* **2002**, *8*, 1405–1411. [[CrossRef](#)]
16. Dubray, O.; Seyed, M.A.; Chen, C.H.; Charbonnier, B.; Descos, A.; Fiorentino, M.; Beausoleil, R.G.; Menezo, S. 30 Gbit/s PAM-4 transmission by modulating a dual silicon ring resonator modulator. In Proceedings of the Optical Interconnects Conference, San Diego, CA, USA, 9–11 May 2016.
17. Luo, L.; Wiederhecker, G.S.; Cardenas, J.; Poitras, C.; Lipson, M. High quality factor etchless silicon photonic ring resonators. *Opt. Express* **2011**, *19*, 6284–6289. [[CrossRef](#)] [[PubMed](#)]
18. Griffith, A.; Cardenas, J.; Poitras, C.B.; Lipson, M. High quality factor and high confinement silicon resonators using etchless process. *Opt. Express* **2012**, *20*, 21341–21345. [[CrossRef](#)] [[PubMed](#)]
19. Dong, P.; Qian, W.; Liao, S.; Liang, H.; Kung, C.; Feng, N.; Shafiihi, R.; Fong, J.; Feng, D.; Krishnamoorthy, A.V.; et al. Low loss shallow-ridge silicon waveguides. *Opt. Express* **2010**, *18*, 14474–14479. [[CrossRef](#)] [[PubMed](#)]
20. Guill, M.A.; Caverley, M.; Cretu, E.; Jaeger, N.A.F.; Chrostowski, L. Large-Area, High-Q SOI Ring Resonators. *IEEE Photon. Conf. IPC* **2014**, *4*, 336–337.
21. Burla, M.; Crockett, B.; Chrostowski, L.; Azaña, J. Ultra-high Q multimode waveguide ring resonators for microwave photonics signal processing. In Proceedings of the International Topical Meeting on Microwave Photonics, Paphos, Cyprus, 26–29 October 2015.
22. Zhang, Y.; Hu, X.; Chen, D.; Wang, L.; Li, M.; Feng, P.; Xiao, X.; Yu, S. Design and demonstration of ultra-high-Q silicon microring resonator based on a multi-mode ridge waveguide. *Opt. Lett.* **2018**, *43*, 1586–1589.
23. Zhang, L.; Jie, L.; Zhang, M.; Wang, Y.; Xie, Y.; Shi, Y.; Dai, D. Ultrahigh-Q silicon racetrack resonators. *Photon. Res.* **2020**, *8*, 684–689. [[CrossRef](#)]
24. Biberman, A.; Shaw, M.J.; Timurdogan, E.; Wright, J.B.; Watts, M.R. Ultralow-loss silicon ring resonators. *Opt. Lett.* **2012**, *37*, 4236–4238. [[CrossRef](#)] [[PubMed](#)]
25. Nezhad, M.P.; Bondarenko, O.; Khajavikhan, M.; Simic, A.; Fainman, Y. Etch-free low loss silicon waveguides using hydrogen silsesquioxane oxidation masks. *Opt. Express* **2011**, *19*, 18827–18832. [[CrossRef](#)] [[PubMed](#)]
26. Bellegarde, C.; Pargon, E.; Sciancalepore, C.; Petit-Etienne, C.; Hugues, V.; Robin-Brosse, D.; Hartmann, J.; Lyan, P. Improvement of Sidewall Roughness of Submicron SOI Waveguides by Hydrogen Plasma and Annealing. *IEEE Photon. Technol. Lett.* **2018**, *30*, 591–594. [[CrossRef](#)]
27. Horikawa, T.; Shimura, D.; Mogami, T. Low-loss silicon wire waveguides for optical integrated circuits. *MRS Commun.* **2016**, *6*, 9–15. [[CrossRef](#)]
28. Frankis, H.C.; Mirabbas Kiani, K.; Bonneville, D.B.; Zhang, C.; Norris, S.; Mateman, R.; Leinse, A.; Bassim, N.D.; Knights, A.P.; Bradley, J.D.B. Low-loss TeO₂-coated Si₃N₄ waveguides for application in photonic integrated circuits. *Opt. Express* **2019**, *27*, 12529–12540. [[CrossRef](#)]
29. Mirabbas Kiani, K.; Frankis, H.C.; Mbonde, H.M.; Mateman, R.; Leinse, A.; Knights, A.P.; Bradley, J.D.B. Thulium-doped tellurium oxide waveguide amplifier with 7.6 dB net gain on a silicon nitride chip. *Opt. Lett.* **2019**, *44*, 5788–5791. [[CrossRef](#)]
30. Mirabbas Kiani, K.; Frankis, H.C.; Mateman, R.; Leinse, A.; Knights, A.P.; Bradley, J.D.B. Thulium-doped tellurium oxide microring lasers integrated on a low-loss silicon nitride platform. *Opt. Mater. Express* **2021**, *11*, 3656–3665. [[CrossRef](#)]
31. Jha, A.; Richards, B.; Jose, G.; Teddy-Fernandez, T.; Joshi, P.; Jiang, X.; Lousteau, J. Rare-earth ion doped TeO₂ and GeO₂ glasses as laser materials. *Prog. Mater. Sci.* **2012**, *57*, 1426–1491. [[CrossRef](#)]
32. Mirabbas Kiani, K.; Frankis, H.C.; Naraine, C.M.; Bonneville, D.B.; Knights, A.P.; Bradley, J.D.B. Lasing in a hybrid rare-earth silicon microdisk. *Laser Photon. Rev.* **2022**, *16*, 210034. [[CrossRef](#)]
33. Preston, K.; Schmidt, B.; Lipson, M. Polysilicon photonic resonators for large-scale 3D integration of optical networks. *Opt. Express* **2013**, *15*, 17283–17290. [[CrossRef](#)]
34. Payne, F.P.; Lacey, J.P.R. A theoretical analysis of scattering loss from planar optical waveguides. *Opt. Quantum Electron.* **1994**, *26*, 977–986. [[CrossRef](#)]
35. Hagan, D.E.; Knights, A.P. Mechanisms for optical loss in SOI waveguides for mid-infrared wavelengths around 2 μm. *J. Opt.* **2017**, *19*, 025801. [[CrossRef](#)]

36. Yap, K.P.; Delâge, A.; Lapointe, J.; Lamontagne, B.; Schmid, J.H.; Waldron, P.; Syrett, B.A.; Janz, S. Correlation of Scattering Loss, Sidewall Roughness and Waveguide Width in SiO₂/Si Silicon-on-Insulator (SOI) Ridge Waveguides. *J. Lightwave Technol.* **2009**, *27*, 3999–4008.
37. Shang, H.; Sun, D.; Yu, P.; Wang, B.; Yu, T.; Li, T.; Jiang, H. Investigation for Sidewall Roughness Caused Optical Scattering Loss of Silicon-on-Insulator Waveguides with Confocal Laser Scanning Microscopy. *Coatings* **2020**, *10*, 236. [[CrossRef](#)]
38. Miller, J.W.; Chesaux, M.; Deligiannis, D.; Mascher, P.; Bradley, J.D.B. Low-loss GeO₂ thin films deposited by ion-assisted alternating current reactive sputtering for waveguide applications. *Thin Solid Films* **2020**, *709*, 13816. [[CrossRef](#)]